The Astrophysical Journal, 923:182 (11pp), 2021 December 20 https://doi.org/10.3847/1538-4357/ac2f45

Role of Parallel Solenoidal Electric Field on Energy Conversion in 2.5D Decaying Turbulence with a Guide Magnetic Field

Peera Pongkitiwanichakul[1], David Ruffolo[2], Fan Guo[3,4], Senbei Du[3], Piyawat Suetrong[1], Chutima Yannawa[1], Kirit Makwana[5], and Kittipat Malakit[6]
[1] Department of Physics, Faculty of Science, Kasetsart University, Bangkok 10900, Thailand; peera.po@ku.th
[2] Department of Physics, Faculty of Science, Mahidol University, Bangkok 10400, Thailand
[3] Los Alamos National Laboratory, Los Alamos, NM 87545, USA
[4] New Mexico Consortium, Los Alamos, NM 87544, USA
[5] Indian Institute of Technology Hyderabad Kandi-502285, Sangareddy Telangana, India
[6] Department of Physics, Faculty of Science and Technology, Thammasat University, Pathum Thani 12120, Thailand
Received 2021 August 28; revised 2021 October 6; accepted 2021 October 11; published 2021 December 21

Abstract

We perform 2.5D particle-in-cell simulations of decaying turbulence in the presence of a guide (out-of-plane) background magnetic field. The fluctuating magnetic field initially consists of Fourier modes at low wavenumbers (long wavelengths). With time, the electromagnetic energy is converted to plasma kinetic energy (bulk flow +thermal energy) at the rate per unit volume of $\boldsymbol{J}\cdot\boldsymbol{E}$ for current density $\boldsymbol{J}$ and electric field $\boldsymbol{E}$. Such decaying turbulence is well known to evolve toward a state with strongly intermittent plasma current. Here we decompose the electric field into components that are irrotational, $\boldsymbol{E}_{\rm ir}$, and solenoidal (divergence-free), $\boldsymbol{E}_{\rm so}$. $\boldsymbol{E}_{\rm ir}$ is associated with charge separation, and $\boldsymbol{J}\cdot\boldsymbol{E}_{\rm ir}$ is a rate of energy transfer between ions and electrons with little net change in plasma kinetic energy. Therefore, the net rate of conversion of electromagnetic energy to plasma kinetic energy is strongly dominated by $\boldsymbol{J}\cdot\boldsymbol{E}_{\rm so}$, and for a strong guide magnetic field, this mainly involves the component $\boldsymbol{E}_{\rm so,\parallel}$ parallel to the total magnetic field $\boldsymbol{B}$. We examine various indicators of the spatial distribution of the energy transfer rate $J_\parallel\cdot E_{\rm so,\parallel}$, which relates to magnetic reconnection, the best of which are (1) the ratio of the out-of-plane electric field to the in-plane magnetic field, (2) the out-of-plane component of the nonideal electric field, and (3) the magnitude of the estimate of current helicity

Unified Astronomy Thesaurus concepts: Plasma physics (2089); Solar magnetic reconnection (1504); Interplanetary turbulence (830)

1. Introduction

The conversion of magnetic field energy into internal energy of plasmas in weakly collisional or collisionless plasmas is not fully understood and has important implications for space plasma and astrophysical plasma phenomena (Parashar et al. 2015). A magnetic field in a nonpotential form can serve as a source of energy for plasma heating and/or particle acceleration in numerous space, solar and astrophysical processes such as coronal heating (Van Ballegooijen 1986; Parker 1988; Pongkitiwanichakul et al. 2015), solar flares (Li et al. 2017; Chen et al. 2020; Fu et al. 2020), solar wind acceleration (De Pontieu et al. 2007), and flares in relativistic jets (Guo et al. 2015; Zhang et al. 2015; Comisso & Sironi 2018; Zhang et al. 2018, 2020). These events involve multiple phenomena operating on a wide range of scales. At large scales, the plasma behaves like a fluid and nonlinear interactions such as turbulence can cause an energy cascade toward small scales where kinetic physics becomes important (Leamon et al. 1998; Gary & Borovsky 2004; Sahraoui et al. 2009; Chandran et al. 2010; Perri et al. 2012; Wan et al. 2012; TenBarge & Howes 2013). While the overall energy conversion rate can be controlled by turbulence at large scales (Wu et al. 2013; Pongkitiwanichakul et al. 2015), unclear mechanisms at kinetic scales determine the proportion of energy transferred to ions or electrons. Ions gain much more energy than electrons in high-energy turbulent astrophysical systems (Zhdankin et al. 2019). Changing the level of fluctuation at kinetic scales causes a change in dominant heating mode. For a higher amplitude of fluctuation, ions gain energy more effectively, while a lower amplitude supports more electron heating (Gary et al. 2016; Hughes et al. 2017; Shay et al. 2018).

A number of recent works searched for the responsible mechanisms and the locations for the energy conversion by using the statistics of properties of the energy transfer rate per unit volume from electromagnetic energy to plasma energy, $\boldsymbol{J}\cdot\boldsymbol{E}$, where $\boldsymbol{J}$ is a current density and $\boldsymbol{E}$ is an electric field. Some previous studies explored how different components of $\boldsymbol{J}\cdot\boldsymbol{E}$ contribute to the total conversion rate. For example, one can consider the perpendicular component of $\boldsymbol{J}$ as the sum of multiple currents due to the anisotropic and nonuniform pressure tensor, such as the grad-B current, the curvature current, and the polarization current (Dahlin et al. 2014; Li et al. 2017, 2018, 2019a). In the case of large-scale magnetic reconnection, $\boldsymbol{J}\cdot\boldsymbol{E}$ from the curvature current dominates. In the case of decaying turbulence with no dominant magnetic reconnection site, the currents are also intermittent and form sheet-like structures (Camporeale et al. 2018). For this case, the main contribution to $\boldsymbol{J}\cdot\boldsymbol{E}$ comes from the interactions between particles and the parallel component of the electric field (Wan et al. 2012; Makwana et al. 2017). Another line of work has considered the conversion into internal energy due to the interaction between the pressure tensor and gradient of the

Figure 1. Schematic of the net energy transfer between the magnetic field, the electric field, and particles via $\langle \boldsymbol{B}\cdot\nabla\times\boldsymbol{E}_{\rm so}/\mu_0\rangle$ and $\langle \boldsymbol{J}\cdot\boldsymbol{E}\rangle$. According to our simulation results, for decaying 2.5D turbulence the two net energy transfer rates are nearly equal, and the net transfer $\langle \boldsymbol{J}\cdot E\rangle$ is dominated by the solenoidal component $\langle \boldsymbol{J}\cdot E_{\rm so}\rangle$.

components of bulk flows (Yang et al. 2017a, 2017b; Du et al. 2018, 2020).

Examination of the spatial distribution, species contributions, and directional components of $\boldsymbol{J}\cdot\boldsymbol{E}$ is useful for understanding how a magnetic field loses its energy to particles. Furthermore, we point out the utility of decomposing $\boldsymbol{E}$ into irrotational ($\boldsymbol{E}_{\rm ir}$) and solenoidal (divergence-free, $\boldsymbol{E}_{\rm so}$) components. The irrotational component arises from the charge separation between ions and electrons. Consider the rates of change of magnetic field and electric field energy according to Maxwell's equations:

$$\frac{\partial}{\partial t}\left(\frac{B^2}{2\mu_0}\right) = -\frac{1}{\mu_0}\boldsymbol{B}\cdot\nabla\times\boldsymbol{E} \tag{1}$$

$$\frac{\partial}{\partial t}\left(\frac{\epsilon_0 E^2}{2}\right) = \frac{1}{\mu_0}\boldsymbol{E}\cdot\nabla\times\boldsymbol{B} - \boldsymbol{J}\cdot\boldsymbol{E}. \tag{2}$$

The first term on the right-hand side of Equation 2 has the same spatial average as the negative of the right-hand side of Equation 1, which represents the rate of conversion of magnetic energy to electric energy. From Equation 1, the irrotational component does not contribute to the time evolution of the magnetic field. In that sense, it cannot exchange energy with the magnetic field. Only the solenoidal component $\boldsymbol{E}_{\rm so}$ can directly drain energy from the magnetic field. Figure 1 shows an illustration of how overall energy is converted between the magnetic field, electric field, and particle kinetic energy (of both bulk flow and thermal energy). The energy density conversion rate between the magnetic field and the electric field is $\boldsymbol{B}\cdot\nabla\times\boldsymbol{E}_{\rm so}/\mu_0$, while $\boldsymbol{J}\cdot\boldsymbol{E}$ is the energy density conversion rate between the electric field and particles. The characteristics of $\boldsymbol{E}_{\rm so}$ control the energy conversion between the magnetic field and the electric field. As will be discussed shortly, our simulation results show that the energy density in the electric field remains low with a very slow rate of change, compared to the magnetic energy or kinetic energy.

Furthermore, we find that the spatial average $\langle \boldsymbol{J}\cdot E_{ir}\rangle$ is very low. Therefore, the net energy flow is from the magnetic field through the solenoidal electric field energy and then, at about the same rate, through to the particle kinetic energy via $\boldsymbol{J}\cdot E_{\rm so}$. In other words, $\boldsymbol{E}_{\rm so}$ controls the flow of magnetic energy to particle kinetic energy, with a spatial distribution marked by $\boldsymbol{J}\cdot E_{\rm so}$. The analyses of $\boldsymbol{J}\cdot\boldsymbol{E}$ from previous studies generally included a major contribution from $\boldsymbol{E}_{\rm ir}$, which may obscure the net energy conversion mechanism and spatial distribution.

In this work, we investigate how the magnetic energy is converted into the kinetic energy of particles. We run particle-in-cell simulations for cases of 2.5 dimensional (2.5D) decaying turbulence with an initially uniform guide magnetic field. The purpose of studying decaying turbulence is to study the evolution of turbulence without the strong influence of the turbulent energy input (forcing) that would have to be added ad hoc to maintain a steady state. Simulations in 2.5D are useful for effectively utilizing computational resources, particularly for the case of a strong guide field, where the turbulent dynamics involve stronger spatial variations along the two directions perpendicular to that field (Montgomery 1982), i.e., they have a quasi-2D nature. We analyze the behavior of $\boldsymbol{J}\cdot\boldsymbol{E}$ from ions and electrons separately. We use Helmholtz decomposition (Kida & Orszag 1992; Yang et al. 2021) to separate the electric field into the irrotational component and the solenoidal component. We focus on how the solenoidal component drains energy out of the magnetic field and find which types of particles gain energy from this component. We consider multiple magnitudes of the guide field and observe how the energy conversion is modified. We find that the simulations have two phases. In the early phase, magnetic islands are formed. In the later phase, these magnetic islands merge. As plasma dynamics in the later phase is less sensitive to the initial conditions and more closely related to astrophysical applications, we focus on the energy transfer in this phase. In the later phase, the interaction between particles and the parallel component of the solenoidal electric field is the main mechanism to drain energy out of the magnetic field in the case of a strong guide field. The interaction is strongly localized, and we find that three good indicators of the spatial locations are (1) the ratio of the out-of-plane electric field to the in-plane magnetic field, (2) the out-of-plane component of the nonideal electric field, and (3) the magnitude of the estimate of current helicity.

2. Simulation Setup

Simulations presented here were performed using VPIC (Bowers et al. 2008), which is an explicit particle-in-cell (PIC) code that has been used to study magnetic reconnection (Daughton et al. 2011; Guo et al. 2020, 2021), turbulence (Wan et al. 2015), and particle energization (Guo et al. 2014, 2015, 2019; Li et al. 2019b). The simulations are 2.5D with y as the ignorable coordinate. The initial magnetic field is the sum of a uniform guide magnetic field and an additional in-plane magnetic field in the form of several Fourier modes with a certain range of wavenumbers:

$$\boldsymbol{B}(x,z) = B_0\hat{y} + \boldsymbol{\delta b}(x,z), \tag{3}$$

where

$$\boldsymbol{\delta b}(x,z) = \sum_{n=1}^{8}\sum_{m=1}^{8}\boldsymbol{b}(n,m)e^{i(2\pi nx/L+2\pi mz/L+\phi_{\rm mn})}, \tag{4}$$

$B_0\hat{y}$ is the uniform guide field and L is the dimension of the cubical box. The wavenumber components along the x and z directions vary from $2\pi/L$ to $16\pi/L$. The phases $\phi_{\rm mn}$ are

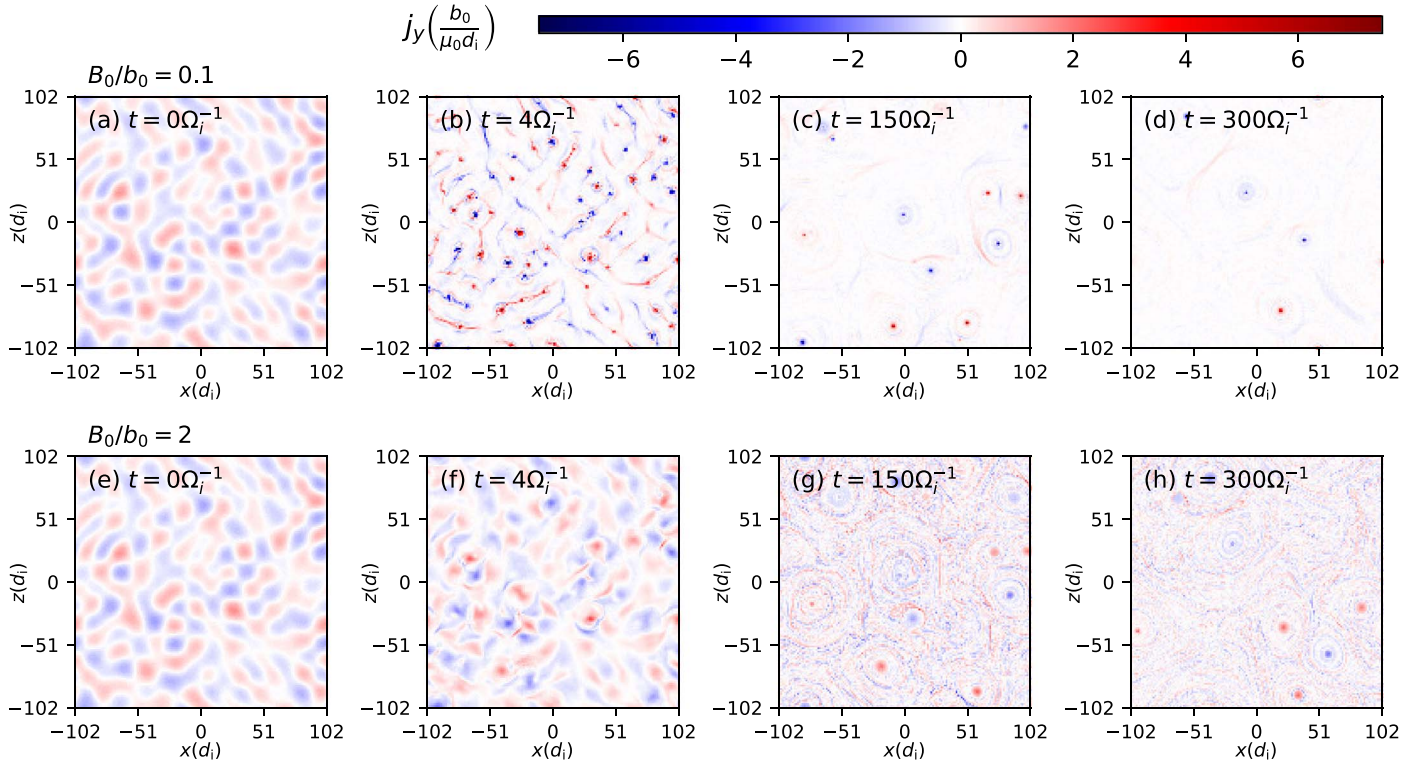

Figure 2. The y-component of the current density at $\Omega_i t = 0$, 4, 150, and 300 from the simulations with $m_i/m_e = 25$ and $B_0/b_0 = 0.1$ (top) and $B_0/b_0 = 2$ (bottom).

randomized. The Fourier coefficient $\boldsymbol{b}(n, m)$ is initially in the x-z plane and is perpendicular to the corresponding wavenumber to maintain $\nabla \cdot \boldsymbol{B} = 0$. The magnitude of $\boldsymbol{b}(n, m)$ is uniform and is set to give $\langle \boldsymbol{\delta b}^2 \rangle = b_0^2$, where b_0 is the unit of the magnetic field in the simulations. This form of the magnetic field is associated with plasma current along the $+y$ and $-y$ directions and contains a total energy available for energy conversion of equal to $(\langle B^2 \rangle - B_0^2)L^3/(2\mu_0) = b_0^2 L^3/(2\mu_0)$. There is no initial electric field and the plasma pressure is uniform. Therefore at its early state, the forces in the plasma are extremely unbalanced.

The plasma consists of ion-electron pairs with the ion-to-electron mass ratio m_i/m_e of 25 or 100. The initial particle distributions are Maxwellian with a uniform density n_0 and a uniform temperature for ions and electrons. The initial electron thermal speed is $0.2c$. The initial bulk flow velocities of ions and electrons give a net-zero mass flow but provide the current density $\boldsymbol{J} = \nabla \times \boldsymbol{B}/\mu_0$. The unit of time is the nominal inverse ion cyclotron frequency for the in-plane magnetic field, $\Omega_{\rm i}^{-1} = m_{\rm i}/(q_{\rm i} b_0)$ and the unit of length is the initial ion inertial length $d_i = c/\omega_{\rm pi}$, where $\omega_{\rm pi}$ is the initial ion plasma frequency. The initial density n_0 is set so that the initial electron plasma frequency is $\omega_{\rm pe} = \Omega_{\rm e} = q_{\rm e} b_0/m_{\rm e}$.

For $m_i/m_e = 25$, we ran simulations with $B_0/b_0 = 0.1$, 0.5, 1, and 2. For $m_i/m_e = 100$, the simulation is with $B_0/b_0 = 2$. Therefore, the initial values of plasma beta range from 0.016 to 0.08. The domain size is $L \times L \times L = 102.4 d_{\rm i} \times 102.4 d_{\rm i} \times 102.4 d_{\rm i}$. The resolution of the simulations is $N_x \times N_y \times N_z = 2048 \times 1 \times 2048$ for $m_i/m_e = 25$ and $4096 \times 1 \times 4096$ for $m_i/m_e = 100$. The number of macroparticles for each species per cell is 400. Periodic boundary conditions are used. Initially, the magnetic fluctuation in all simulations contains the total energy of $5.4 \times 10^5\, b_0^2 d_i^3/\mu_0$. Simulations were run until the magnetic free energy dropped to ∼12% of the total energy from the initial magnetic fluctuation. All our reported results are for $m_i/m_e = 25$ except where noted.

3. Results

3.1. Plasma Dynamics

Figure 2 shows the y-component of the current density, j_y, at $\Omega_i t = 0$, 4, 150, and 300 from the simulations with $B_0/b_0 = 0.1$ and 2. The initial plasma configuration is unstable since the forces are extremely imbalanced. At this early time, the plasma flow is highly compressible as current structures contract to form magnetic islands. Figure 3(a) shows the compressible fraction of the ion flow energy $\langle U_{\rm i,ir}^2 \rangle / \langle U_{\rm i}^2 \rangle$, which is the ratio of the kinetic energy of the compressible (irrotational) ion flow $U_{\rm i,ir}$ to the total kinetic energy of the ion flow $U_{\rm i}$. This ratio quickly rises at the beginning and reaches a maximum value greater than 0.8 after a few ion cyclotron times in all simulations. Later, the ratio declines and remains fairly stationary after $\Omega_{\rm i}\tau = 5$ (dashed line). The current contraction also builds free energy in B_y as shown in Figure 3(b). From the simulations, the magnitude of $B_y - B_0$ is high at the centers of the magnetic islands. After a few ion cyclotron times, the current within each flux rope contracts, reducing energy in the magnetic field. Multiple major magnetic islands become obvious after the contraction of plasma currents inside each island as shown in Figure 2 at $\Omega_{\rm i} t = 4$, 150, and 300.

The conditions at $t \lesssim \tau$, the island-forming phase, involve imbalanced forces that reflect the initial condition and are unlikely to appear in nature.

At $t \gtrsim \tau$, the current-merging or decaying phase, the forces are only weakly imbalanced, and the rms of current density reaches its maximum value at $\Omega_{\rm i} t = 25$. In this phase, multiple

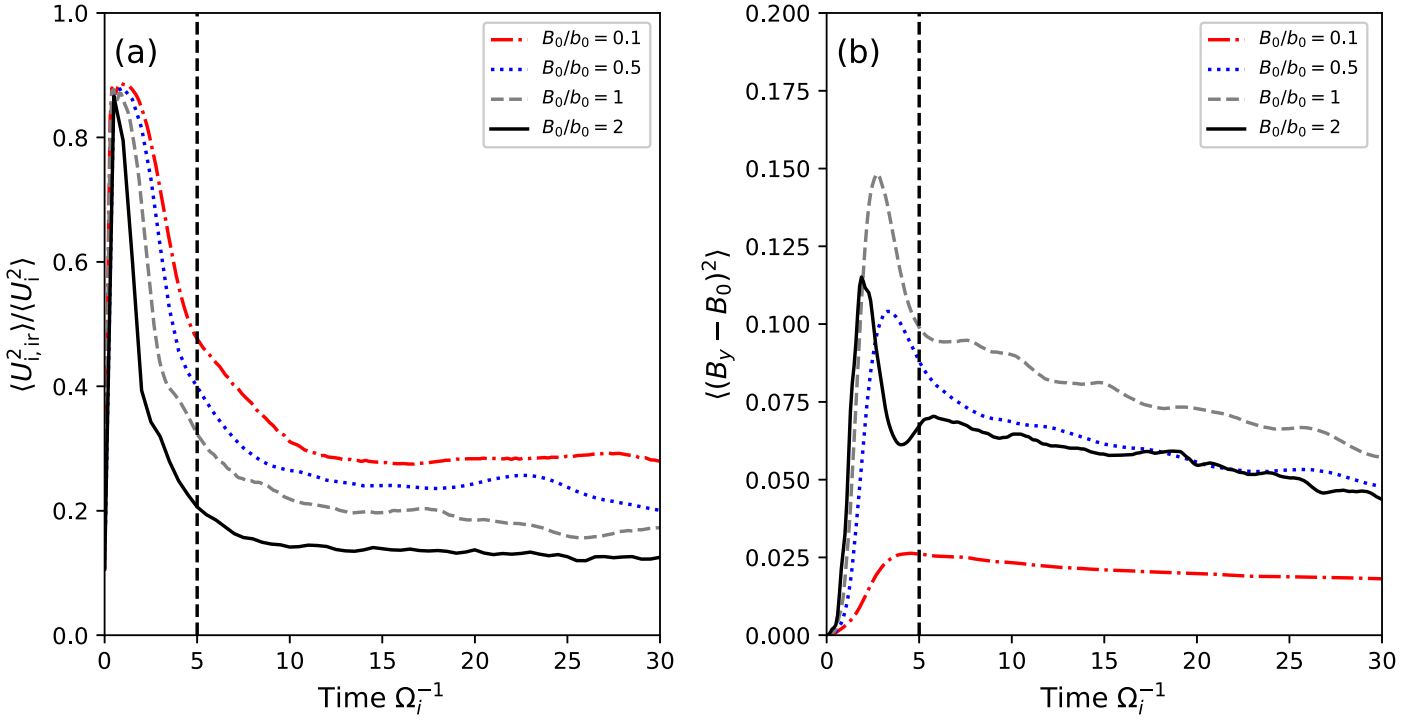

Figure 3. (a) Compressible fraction of the ion flow energy $\langle U_{i,ir}^2 / U_i^2 \rangle$ as a function of time. (b) Spatial average of the square of the magnetic fluctuation in the y direction, i.e., the free energy of the guide magnetic field. The dashed line indicates time τ between the island-forming and decay phases.

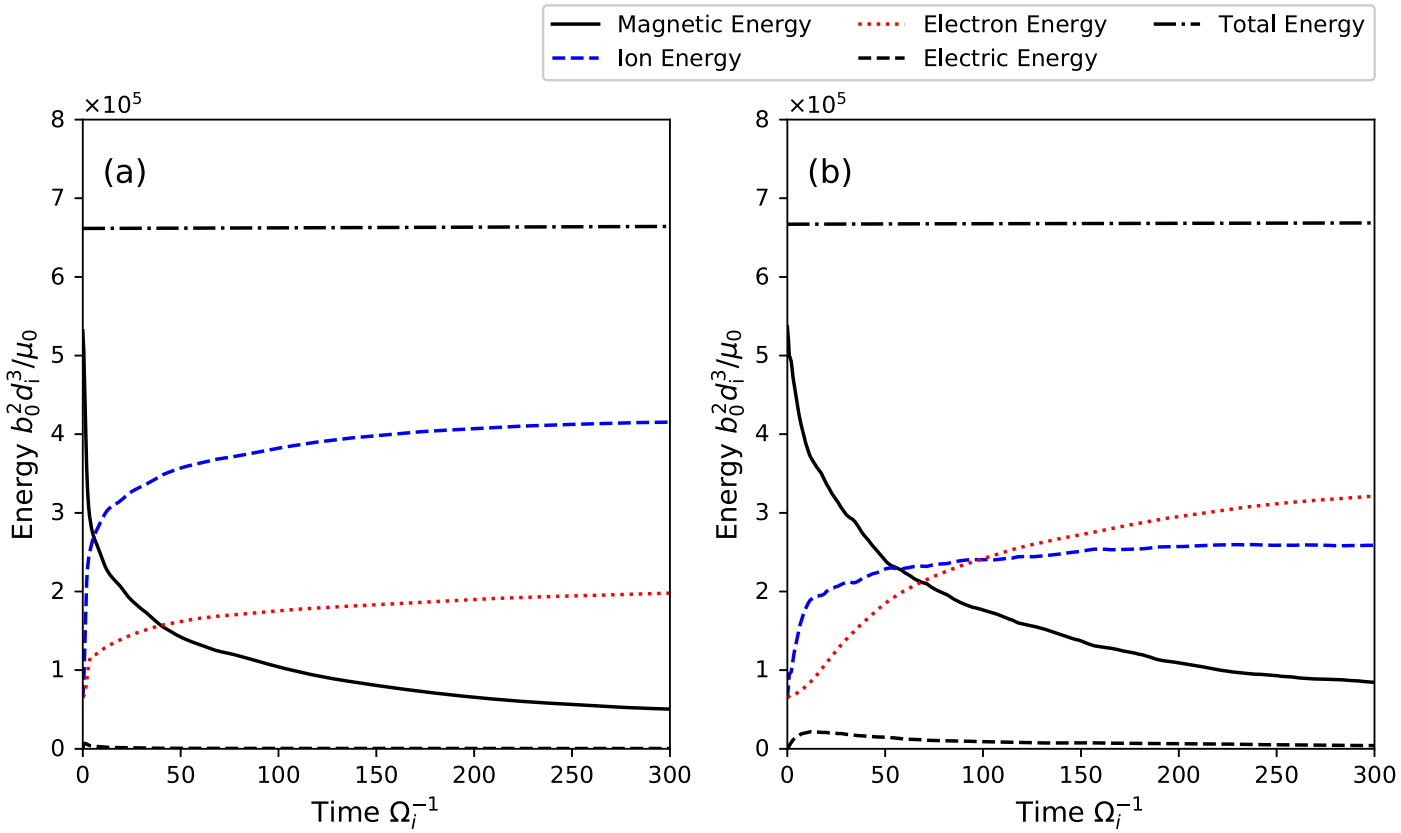

Figure 4. Time series of the total magnetic fluctuation energy, total electric energy, total ion energy, total electron energy, total transferable energy and (a) $B_0/b_0 = 0.1$ and (b) $B_0/b_0 = 2$.

magnetic islands merge as the currents sharing the same direction attract one another. Before the merging of two islands is complete, a current sheet emerges between them and becomes a site for magnetic reconnection accompanied with a number of small islands. This phase is more applicable to natural situations in space plasmas. For stronger B_0, there are

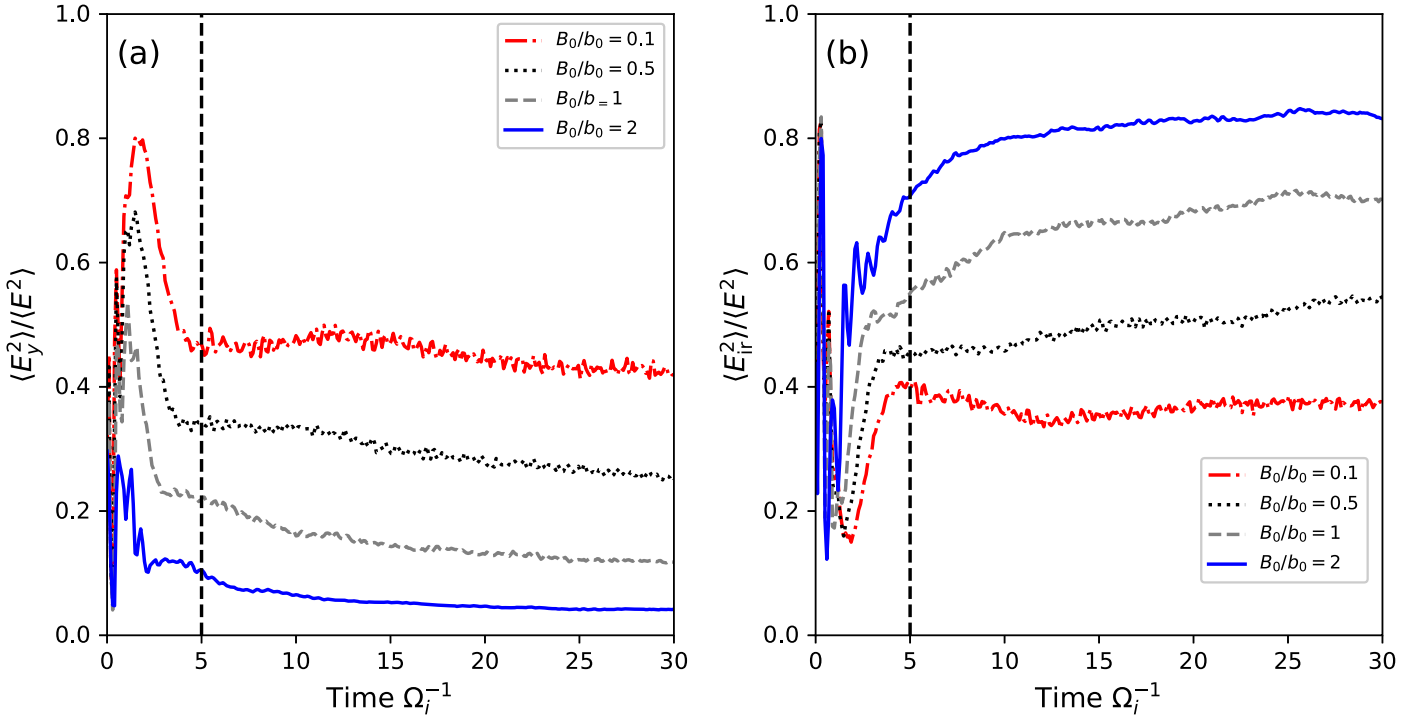

Figure 5. Fraction of electric energy in the (a) y-component and (b) irrotational component as a function of time. The dashed line indicates time τ between island-forming and decaying phases.

more of these tiny islands; see the plots of j_y at $\Omega_i t = 150$ and 300 in Figure 2. These emerging plasmoids from the reconnection have a short lifetime as they are destroyed by smaller-scale magnetic reconnection after colliding with the surrounding plasma. As the current merging continues, there are fewer sites for magnetic reconnection and associated plasma activity

3.2. Energy Conversion Profiles

3.2.1. Overview

Figure 4 shows the magnetic fluctuation energy, electric field energy, total ion energy, total electron energy, and total transferable energy as time series from the simulations with $B_0/b_0 = 0.1$ and 2. The electric energy is tiny and nearly constant, so it does not serve as a significant source or sink of energy, and referring to Figure 1, $\boldsymbol{J}\cdot\boldsymbol{E}$ can accurately represent both electric and magnetic energy conversion rates per unit volume. When B_0 changes, the overall amount of energy gained by ions and electrons also changes. Electrons eventually gain more energy for higher B_0 (Gary et al. 2016; Hughes et al. 2017). In our 2.5D simulations, all quantities depend on x and z while y is an ignorable coordinate. By applying Faraday's law to our scenarios, only the y-component of the electric field can modify the in-plane magnetic field while the in-plane electric field can only modify B_y. Since the initial magnetic fluctuation is in the x–z plane, the overall conversion of energy from the magnetic field is well represented by the integral of J_yE_y over space and time. This integration includes magnetic energy lost during the island-forming and the decaying phases.

At $t \lesssim \tau$, energy in B_x and B_z drops via E_y but the energy in B_y increases. During the island-forming phase, $\langle J_yE_y\rangle$ is higher than $\langle \boldsymbol{J}\cdot\boldsymbol{E}\rangle$ because part of the energy from $\langle J_yE_y\rangle$ is used for building strong free energy $\langle (B_y - B_0)^2\rangle$ at centers of the magnetic islands via the in-plane solenoidal electric field $\boldsymbol{E}_{\rm so,xz}$. Therefore, $\langle J_yE_y\rangle$ must be less than $\langle \boldsymbol{J}\cdot\boldsymbol{E}\rangle$ during the decaying phase.

Since the island-forming phase and decaying phase have distinct mechanisms of energy conversion, these can be analyzed separately. As the decaying phase is more applicable to astrophysical situations, we focus more on the energy conversion during this later phase of the simulation. We examine the mechanism that takes energy out of B_y while E_y continues to take energy out of the in-plane components of the magnetic field.

Figure 5(a) shows the ratio of the energy in E_y to the total electric field energy at times up to $30\Omega_i^{-1}$. As B_0 is increased, E_y provides a lower energy fraction at $t \gtrsim \tau$. For $B_0/b_0 = 2$, the energy in E_y is around 5% of the total electric field energy at $t \gtrsim \tau$. Meanwhile, the energy in $\boldsymbol{E}_{\rm ir}$ can be as high as 80% of the total electric field energy for $B_0/b_0 = 2$ at $t \gtrsim \tau$, as shown in Figure 5(b). Since $\boldsymbol{E}_{\rm ir}$ provides a significant fraction of the electric energy, which even dominates at large B_0, a large portion of $\boldsymbol{J}\cdot\boldsymbol{E}$ represents energy exchange between ions and electrons without directly involving the conversion of magnetic energy. The analysis of how $\boldsymbol{J}\cdot\boldsymbol{E}$ take energy out of the magnetic field must consider the large contribution from $\boldsymbol{E}_{\rm ir}$ into account.

3.2.2. Island-forming Phase

First consider $\langle \boldsymbol{J}\cdot\boldsymbol{E}\rangle$ at $t < \tau$. We separately consider the energy transfer to ions and electrons as well as the contributions from $\boldsymbol{E}_{\rm ir}$, $\boldsymbol{E}_{\rm so,xz}$, and E_y to $\langle \boldsymbol{J}\cdot\boldsymbol{E}\rangle$ (Figure 6). (Note that $\boldsymbol{E}_y$ is purely solenoidal.) At $t \lesssim \tau$, simulations with $B_0/b_0 = 0.1$ and 2 both show that electrons are mainly responsible for taking energy out of the in-plane magnetic field via $\boldsymbol{E}_y$. Electrons then transfer most of this energy to ions via $\boldsymbol{E}_{\rm ir}$ (recall that $\boldsymbol{E}_{\rm ir}$ is associated with charge separation) and ions gain more energy than electrons in this phase. The profiles

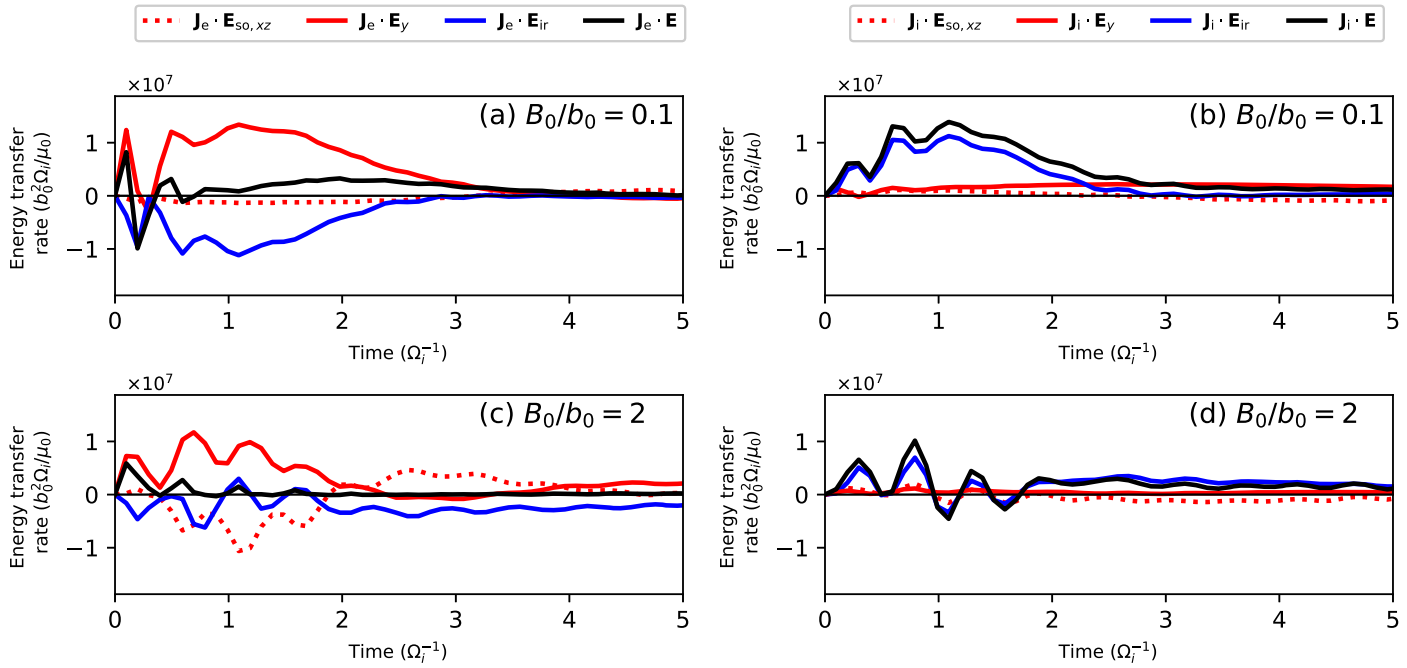

Figure 6. Panels (a) and (b) show the rates of energy transfer to ions and electrons, respectively, for various electric field components with $B_0/b_0 = 0.1$ for $t < \tau$. Panels (c) and (d) show the same rates to ions and electrons, respectively, with $B_0/b_0 = 2$.

of the energy transfer rates to electrons and ions via $\boldsymbol{E}_{\rm ir}$ are very similar but with opposite signs. This implies that the particle interactions with $\boldsymbol{E}_{\rm ir}$ mostly do not store or extract electric energy in $\boldsymbol{E}_{\rm ir}$ but only cause the energy exchange between particles of opposite charges.

For simulations with $m_i/m_e = 25$, and $B_0/b_0 = 0.1$, 0.5, 1, and 2, the total energy $W_{25,1}$ gained by particles during the first (island-forming) phase from the beginning to $t = \tau$ was 2.5×10^5, 1.9×10^5, 1.3×10^5, and 1.0×10^5, respectively, in units of $b_0^2 d_{\rm i}^3/\mu_0$. Less energy is transferred to particles during this phase when B_0 is higher. Table 1 shows the fraction of the total electromagnetic energy transfer to particles that go to ions and electrons via $\boldsymbol{E}_{\rm ir}$, $\boldsymbol{E}_{\rm so,xz}$, E_y, and the total electric field $\boldsymbol{E}$ from the beginning to $t = \tau$, for each simulation.

In all simulations, electrons take energy from the in-plane components of the magnetic field and transfer a large amount of energy to ions via $\boldsymbol{E}_{\rm ir}$. Both ions and electrons lose some energy to form strong $|B_y - B_0|$ at the centers of magnetic islands. As B_0/b_0 is increased up to 1, more energy is transferred to B_y and the energy transfer via $\boldsymbol{E}_{\rm ir}$ is also stronger. At $t = \tau$, ions have gained more energy than electrons even though electrons are the main species interacting with E_y and reducing the magnitude of the in-plane magnetic field.

3.2.3. Decaying Phase

At $t > \tau$, the current contraction is less active. Magnetic energy drops due to the merging of magnetic islands. We carry on the analysis of energy conversion by considering the contributions from ions and electrons, again separating effects of $\boldsymbol{E}_{\rm ir}$ from $\boldsymbol{E}_{\rm so}$. In this phase, we found that separating the solenoidal field into $\boldsymbol{E}_y$ and $\boldsymbol{E}_{\rm so,xz}$ is not the most effective way to understand the energy conversion. In this phase, energy conversion often takes place where both B_y and the in-plane magnetic field lose energy together. We found that separating the solenoidal electric field into the components parallel $\boldsymbol{E}_{\rm so,\parallel}$ and perpendicular $\boldsymbol{E}_{\rm so,\perp}$ to the local magnetic field is more suitable for a strong guide field.[7]

Table 1
The Fractions of the Total Electromagnetic Energy Transfer to Particle Energy that Go To Ions and Electrons during the Island-forming Phase ($t < \tau$) via Interactions with $\boldsymbol{E}_{\rm so,xz}$, E_y, $\boldsymbol{E}_{\rm ir}$, and $\boldsymbol{E}$

B_0/b_0	Species	$\boldsymbol{J}_{\rm s} \cdot \boldsymbol{E}_{\rm so,xz}$	$\boldsymbol{J}_{\rm s} \cdot \boldsymbol{E}_y$	$\boldsymbol{J}_{\rm s} \cdot \boldsymbol{E}_{\rm ir}$	$\boldsymbol{J}_{\rm s} \cdot \boldsymbol{E}$
0.1	Ion	−0.01	0.28	0.52	0.79
	Electron	−0.05	0.78	−0.52	0.21
0.5	Ion	−0.08	0.35	0.55	0.82
	Electron	−0.17	0.92	−0.57	0.18
1	Ion	−0.18	0.30	0.76	0.88
	Electron	−0.26	1.17	−0.79	0.12
2	Ion	−0.24	0.19	0.88	0.83
	Electron	−0.13	1.28	−0.98	0.17

Figures 7(a) and 7(c) show the energy conversion rates to electrons and ions via $\boldsymbol{E}_{\rm so}$ for $B_0/b_0 = 0.1$ and 2, respectively, at $t > \tau$. For $B_0/b_0 = 0.1$, $\langle \boldsymbol{J}_{i,\perp} \cdot \boldsymbol{E}_{\rm so} \rangle$ is positive and dominates other rates. For $B_0/b_0 = 2$, $\langle \boldsymbol{J}_{e,\perp} \cdot \boldsymbol{E}_{\rm so} \rangle$ and $\langle \boldsymbol{J}_{i,\perp} \cdot \boldsymbol{E}_{\rm so} \rangle$ fluctuate with large magnitudes, share similar shapes, and seem to have opposite signs. On the other hand, the rates $\langle \boldsymbol{J}_{e,\parallel} \cdot \boldsymbol{E}_{\rm so} \rangle$ and $\langle \boldsymbol{J}_{i,\parallel} \cdot \boldsymbol{E}_{\rm so} \rangle$ remain mostly positive with smaller magnitudes. The rates from $\boldsymbol{E}_{\rm ir}$ are shown in Figure 7(b) for $B_0/b_0 = 0.1$ and Figure 7(d) for $B_0/b_0 = 2$. These rates fluctuate with stronger magnitude when B_0 is higher. The rates for ions and electrons are nearly equal and opposite almost all the time, representing

[7] We have considered the relevance of components parallel and perpendicular to **B** versus out-of-plane (y) and in-plane (x–z) components for the decaying phase. We found that resolving components parallel and perpendicular to **B** provides a clearer physical distinction for particle acceleration (direct parallel acceleration versus perpendicular drift motion) and also a clearer distinction among components of the pressure tensor.

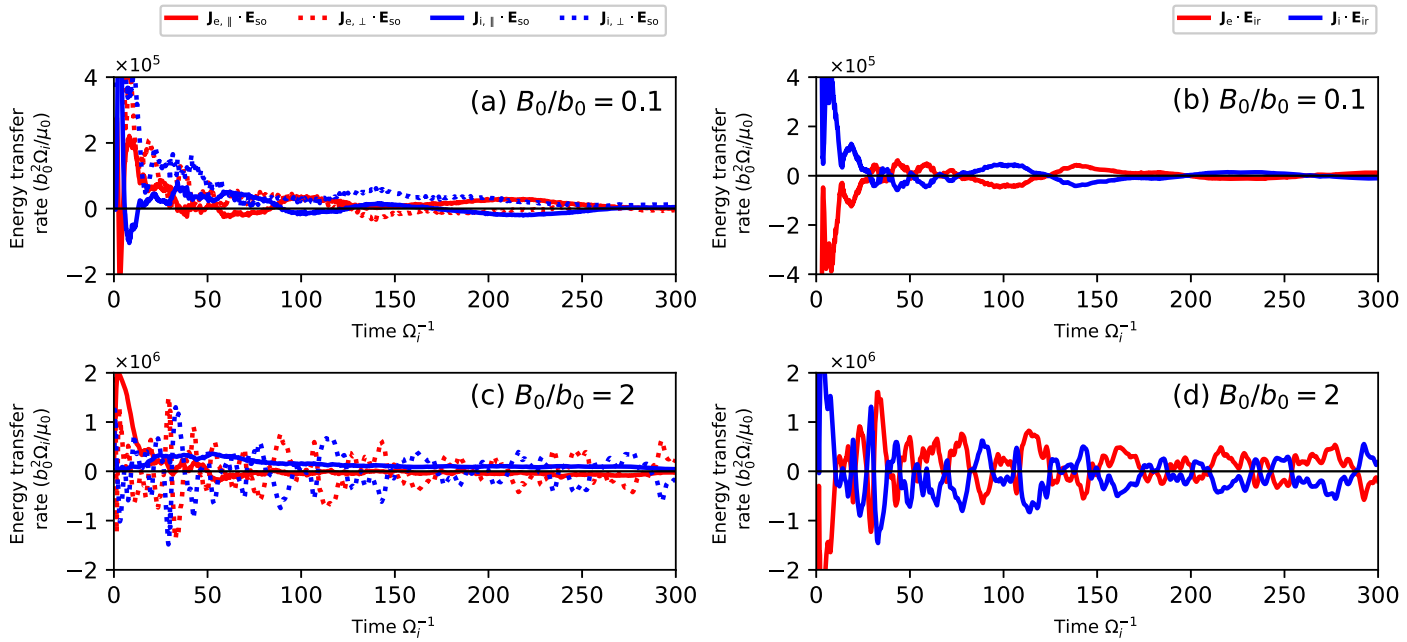

Figure 7. The rates of energy conversion to ions and electrons by interacting with components of (a) $\boldsymbol{E}_{\rm so}$ and (b) $\boldsymbol{E}_{\rm ir}$ from the simulations with $B_0/b_0 = 0.1$. Panels (c) and (d) show the energy conversion rates to ions and electrons from interaction with components of $\boldsymbol{E}_{\rm so}$ and $\boldsymbol{E}_{\rm ir}$, respectively, with $B_0/b_0 = 2$.

energy transfer among particle species with little net conversion of electromagnetic energy to particle motion.

Let $W_{25,2}$ be the total energy gained by particles in the second (decaying) phase after $t = \tau$ for each simulation with $m_i/m_e = 25$. The values are 2.3×10^5, 2.8×10^5, 3.4×10^5, and 3.7×10^5 in units of $b_0^2 d_i^3/\mu_0$ for $B_0/b_0 = 0.1$, 0.5, 1, and 2, respectively. Table 2 shows the fractions of the total energy gain that goes to ions and electrons via $\boldsymbol{E}_{\rm so,\parallel}$, $\boldsymbol{E}_{\rm so,\perp}$, $\boldsymbol{E}_{\rm ir}$, and the total electric field $\boldsymbol{E}$. The values in the table are fractions of $W_{25,2}$. For $B_0/b_0 = 0.1$, the most effective motion to transfer energy via $\boldsymbol{E}_{\rm so}$ is the perpendicular motion of ions. This motion takes $0.51W_{25,2}$ of the converted energy while the parallel and the perpendicular motions of electrons take $\sim 0.20W_{25,2}$ each. The interaction between ions and electrons via $\boldsymbol{E}_{\rm ir}$ is weak. The total amounts of energy gained by ions and electrons for $t > \tau$ are $0.65W_{25,2}$ and $0.35W_{25,2}$, respectively. For small B_0 at $t > \tau$, the energy transferred via $\boldsymbol{E}_y$ still dominates and 92% of electromagnetic energy conversion is via $\boldsymbol{E}_y$. Therefore, separating the rates from $\boldsymbol{E}_{\rm so,\parallel}$ and $\boldsymbol{E}_{\rm so,\perp}$ is not particularly useful. As B_0 increases, the parallel motion of ions becomes the most effective motion to take energy from $\boldsymbol{E}_{\rm so}$. The particle interaction through $\boldsymbol{E}_{\rm ir}$ is also stronger as $\boldsymbol{E}_{\rm ir}$ is stronger for higher B_0. For $B_0/b_0 = 2$, the parallel motion of ions takes $0.91W_{25,2}$ from $\boldsymbol{E}_{\rm so}$ while $\boldsymbol{E}_{\rm ir}$ takes $0.67W_{25,2}$ from ions and gives $0.68W_{25,2}$ to electrons. For $t > \tau$, the energy gained by electrons is $0.73W_{25,2}$ while ions gain only $0.27W_{25,2}$. As B_0 increases, the energy conversion by the parallel electric field becomes stronger. For $B_0/b_0 = 2$, $\boldsymbol{E}_{\rm so,\parallel}$ is responsible for almost 100% of $W_{25,2}$, while E_y takes 88% of $W_{25,2}$ out of the magnetic field. The dominance of $\boldsymbol{E}_{\rm so,\parallel}$ implies that energy in B_y and the in-plane magnetic field are likely drained at the same locations via $\boldsymbol{E}_{\rm so,\parallel}$.

For comparison, we calculate the energy conversion via $\boldsymbol{E}_{\rm so,\parallel}$ and $\boldsymbol{E}_{\rm so,\perp}$ in Table 3 for $t < \tau$. For $B_0/b_0 = 0.1$, the magnetic field lies mostly in the x-z plane initially and the perpendicular direction is nearly along the y direction. Therefore, in the first phase, the sum of $\boldsymbol{J}_\perp\cdot\boldsymbol{E}_{\rm so,\perp}$ from both species, with E_y as the main component in $\boldsymbol{E}_{\rm so,\perp}$, is responsible for 95% of the energy conversion. For the case of $B_0/b_0 = 2$, the initial magnetic field tends to be more aligned with the y direction. As E_y is the main component of $\boldsymbol{E}_{\rm so,\parallel}$, the sum of $\boldsymbol{J}_\parallel\cdot\boldsymbol{E}_{\rm so,\parallel}$ from both species is responsible for 89% of the energy conversion. Thus these

Table 2
The Fraction of the Total Electromagnetic Energy Transfer to Particle Energy that Go To Ions and Electrons via Interactions with $\boldsymbol{E}_{\rm so,\parallel}$, $\boldsymbol{E}_{\rm so,\perp}$, $\boldsymbol{E}_{\rm ir}$, and $\boldsymbol{E}$ during the Decaying Phase ($t > \tau$)

B_0/b_0	Species	$\boldsymbol{J}_{\rm s,\parallel}\cdot\boldsymbol{E}_{\rm so,\parallel}$	$\boldsymbol{J}_{\rm s,\perp}\cdot\boldsymbol{E}_{\rm so,\perp}$	$\boldsymbol{J}_{\rm s}\cdot\boldsymbol{E}_{\rm ir}$	$\boldsymbol{J}_{\rm s}\cdot\boldsymbol{E}$
0.1	Ions	0.04	0.51	0.10	0.65
	Electrons	0.20	0.23	−0.08	0.35
0.5	Ions	0.63	0.02	−0.07	0.58
	Electrons	0.16	0.18	0.08	0.42
1	Ions	1.21	−0.01	-0.68	0.52
	Electrons	−0.27	0.05	0.70	0.48
2	Ions	0.91	0.03	−0.67	0.27
	Electrons	0.10	−0.05	0.68	0.73

Table 3
The Fraction of the Total Electromagnetic Energy Transfer to Particle Energy that Go To Ions and Electrons via Interactions with $\boldsymbol{E}_{\rm so,\parallel}$ and $\boldsymbol{E}_{\rm so,\perp}$ for the Island-forming Phase ($t < \tau$)

B_0/b_0	Species	$\boldsymbol{J}_{\rm s,\parallel}\cdot\boldsymbol{E}_{\rm so,\parallel}$	$\boldsymbol{J}_{\rm s,\perp}\cdot\boldsymbol{E}_{\rm so,\perp}$
0.1	Ions	0.06	0.21
	Electrons	≈ 0	0.73
0.5	Ions	0.01	0.26
	Electrons	0.23	0.52
1	Ions	−0.02	0.14
	Electrons	0.48	0.43
2	Ions	0.03	−0.08
	Electrons	0.86	0.29

results are consistent with our conclusion from the previous section that E_y plays the dominant role in energy conversion for $t < \tau$ (see Table 1).

The energy transfer processes in the phases $t < \tau$ and $t > \tau$ are very different. Electrons are the main species to draw energy from the magnetic field in the early phase but lose most of the energy to ions via the charge separation and $\boldsymbol{E}_{\rm ir}$. In the later phase, ions are more responsible for draining energy from the magnetic field. For $B_0/b_0 = 0.5$, 1, and 2, these ions lose energy to electrons via the charge separation and $\boldsymbol{E}_{\rm ir}$. The interaction between ions and electrons via $\boldsymbol{E}_{\rm ir}$ is stronger as B_0 increases. Our analysis is insensitive to choices of the boundary time from $\Omega_i\tau = 5$ to 10. By using $\Omega_i\tau = 10$, the results change numerically but remain qualitatively similar. The results for $m_i/m_e = 100$ are also qualitatively similar to those for $m_i/m_e = 25$.

3.3. Indicators of Energy Conversion Locations

From the previous section, the overall rate of energy transfer to particles in the decaying phase is approximately equal to the integration of $J_\parallel E_{\rm so,\parallel}$ over $t > \tau$. In all the simulations, $\nabla \times \boldsymbol{B} \approx \mu_0 \boldsymbol{J}$ is valid at most locations so we can write

$$J_\parallel E_{\rm so,\parallel} \approx \frac{1}{\mu_0}\boldsymbol{E}_{\rm so,\parallel}\cdot\nabla\times\boldsymbol{B} = \frac{1}{\mu_0}\boldsymbol{B}\cdot\nabla\times\boldsymbol{E}_{\rm so,\parallel}, \quad (5)$$

noting that $\boldsymbol{E}_{\rm so,\parallel}$ is parallel to $\boldsymbol{B}$, so there is no Poynting vector associated with $\boldsymbol{E}_{\rm so,\parallel}$. The last term is the rate of change of the local magnetic energy density due to $\boldsymbol{E}_{\rm so,\parallel}$ from Faraday's law. Therefore, the energy transferred via the parallel motion is local and the magnetic energy quite instantly becomes the kinetic energy of particles, where $\nabla \times \boldsymbol{B} \approx \mu_0 \boldsymbol{J}$.

Figure 8(a) shows the color plot of $J_\parallel E_{\rm so,\parallel}$ over the entire domain at $t = 22\Omega_i^{-1}$ from the simulations with $B_0/b_0 = 2$. Contours of vector potential $A\hat{y}$ are shown in black ($A < 0$) and gray ($A > 0$). In 2D simulations, these curves are also the projection of the magnetic field lines on the x–z plane. The magnetic islands are surrounded by circular closed curves while the current sheets are located at boundaries between magnetic islands that share the same rotation direction. The rate $J_\parallel E_{\rm so,\parallel}$ fluctuates strongly and is highly intermittent in space. The energy is transferred strongly both ways, either from fields to particles ($J_{\rm parallel}E_{\rm so,\parallel} > 0$, red color) or from particles to fields ($J_{\rm parallel}E_{\rm so,\parallel} < 0$, blue color). From the previous sections we have learned that the spatial average of $J_\parallel E_{\rm so,\parallel}$ is positive, indicating a net conversion of energy from fields to particle kinetic energy. We can see two types of structures with strong (positive or negative) values of $J_\parallel E_{\rm so,\parallel}$: (1) Near the centers of magnetic islands, there are bipolar structures, with positive and negative $J_\parallel E_{\rm so,\parallel}$. We have confirmed that the positive and negative values nearly cancel, and these regions make a tiny contribution to the net energy conversion rate $\langle J_\parallel E_{\rm so,\parallel}\rangle$. (2) Near the edges of magnetic islands, there are elongated regions with strong $J_\parallel E_{\rm so,\parallel}$, including regions of magnetic reconnection. The positive values of $J_\parallel E_{\rm so,\parallel}$ dominate and these regions account for the overall positive energy conversion. Therefore, it would be useful to find quantities that indicate these regions near the edges of magnetic islands, especially if they provide some insight into why the energy conversion mostly occurs in these specific locations.

In this section, we examine various quantities as possible indicators of energy conversion locations, and specifically of regions with strong and positive $J_\parallel E_{\rm so,\parallel}$ on average. We test these indicators using the following steps. For any continuous indicator X, we identify the median X_m of X values at all grid points over the spatial domain as a time series (for $t > \tau$). We integrate the total energy $\epsilon_{X,h}$ transferred to particle kinetic energy by $J_\parallel E_{\rm so,\parallel}$ from the region with $X > X_m$ over the time domain of interest and compare $\epsilon_{X,h}$ with the total energy ϵ_X from $J_\parallel E_{\rm so,\parallel}$ over the spatial and time domains. We then calculate a measure of predictive power, $S_X = 2|\epsilon_{X,h}/\epsilon_X - 0.5|$. Because a monotonic transformation of X does not change its percentiles, with this construction, S_x is invariant upon any monotonic transformation of the indicator X, and $0 \leqslant S_X \leqslant 1$. If S_X is close to 1, then X is a good indicator of energy conversion locations.

We have tested many indicators using the data from simulations with $B_0/b_0 = 2$. Table 4 shows a list of indicators and their predictive power regarding energy transferred via $J_\parallel E_{\rm so,\parallel}$ for all times $t > \tau$. We include $|E_{\rm so,\parallel}|$ and $|J_\parallel|$, which multiply to make $|J_\parallel||E_{\rm so,\parallel}|$, only for comparison. We found three good indicators in addition to $|E_{\rm so,\parallel}|$ and $|J_\parallel|$ themselves.

The best such indicator is $|E_y|/|B_{\rm xz}|$, which is based on an indicator suggested by Lapenta (2021). That work actually examined the formal transformation velocity $\boldsymbol{v}_L = c^2\boldsymbol{B}\times\boldsymbol{E}/E^2$ such that a Lorentz transformation would nullify the two components of the magnetic field in the plane perpendicular to the electric field, as an indicator of reconnection regions in 3D space. The magnitude of $\boldsymbol{v}_L$ is almost always superluminal, with $v_L < c$ only in the vicinity of reconnection sites. For our configuration, with a guide magnetic field component B_y, reconnection sites should have $\boldsymbol{B}_{\rm xz} \approx 0$ and we can simply use $v_L = c^2|B_{\rm xz}|/|E_y|$. As a further simplification, we divide v_L by c^2 and invert to obtain $|E_y|/|B_{\rm xz}|$, which has units of velocity and is usually close to zero, but is large near null points of $\boldsymbol{B}_{\rm xz}$ that have nonzero E_y, i.e., near reconnection regions.

We found that $S_{|E_y|/|B_{\rm xz}|}$ is 0.82, i.e., 91% of the energy transferred via $J_\parallel E_{\rm so,\parallel}$ occurs in regions with $|E_y|/|B_{\rm xz}|$ higher than its median value, which are typically near reconnection sites. This indicator has higher predictive power for $J_\parallel E_{\rm so,\parallel}$ than $|E_{\rm so,\parallel}|$ itself.

The second best indicator is the magnitude of the y-component of the nonideal electric field, $\delta E_y = \hat{y}\cdot(\boldsymbol{E} + \boldsymbol{U}\times\boldsymbol{B})$, where $\boldsymbol{U}$ is the plasma bulk velocity. At locations with a high magnitude of $\boldsymbol{E} + \boldsymbol{U}\times\boldsymbol{B}$, the frozen-in approximation is no longer valid. However, we find that the magnitude of $\boldsymbol{E} + \boldsymbol{U}\times\boldsymbol{B}$ is not as good of an indicator as δE_y. We found that $S_{\delta E_y}$ is 0.8, implying that 90% of the energy transferred via $J_\parallel E_{\rm so,\parallel}$ occurs in regions with δE_y above its median value. This indicator has a predictive power for $J_\parallel E_{\rm so,\parallel}$ equal to $|E_{\rm so,\parallel}|$ itself. This implies that strong energy conversion often takes place where the frozen-in approximation fails, which also typically occurs near reconnection sites.

The third best indicator is an estimate $H = |\boldsymbol{B}\cdot\nabla\times\boldsymbol{B}|/\mu_0$ of the current helicity $|\boldsymbol{J}\cdot\boldsymbol{B}|$. We can write

$$J_\parallel E_{\rm so,\parallel} = \frac{E_{\rm so,\parallel}|\boldsymbol{J}\cdot\boldsymbol{B}|}{B}, \quad (6)$$

so the current helicity is directly linked with $J_\parallel E_{\rm so,\parallel}$. We use $H = |\boldsymbol{B}\cdot\nabla\times\boldsymbol{B}|/\mu_0$ as an estimate of the current helicity that only involves magnetic field measurements, as may be more readily available from spacecraft data. We found that S_H is 0.76, implying that 88% of the energy transferred via $J_\parallel E_{\rm so,\parallel}$ occurs in the region with H above its median value.

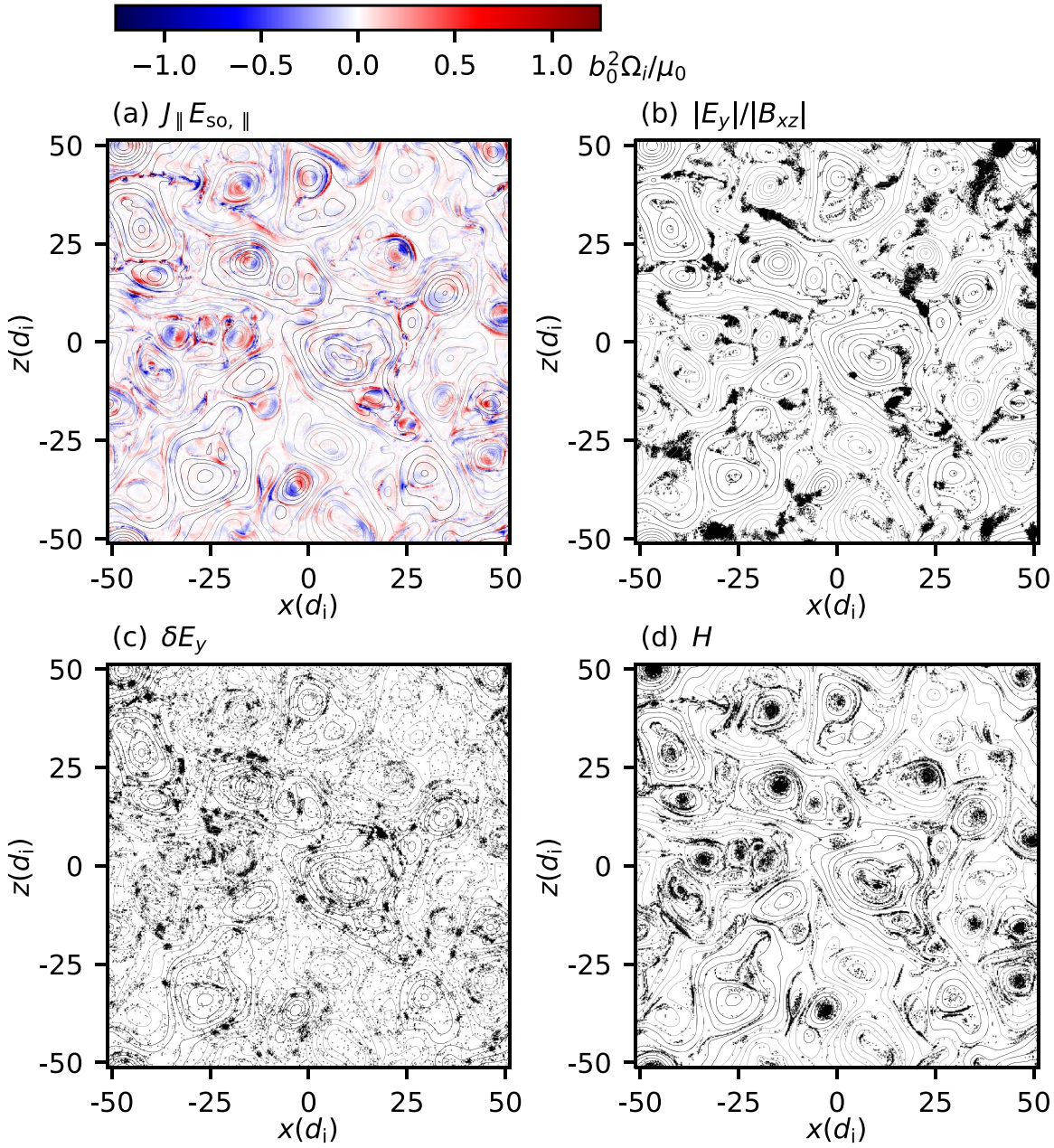

Figure 8. (a) 2D color plot of $J_\parallel E_{so,\parallel}$ at $t = 22\Omega_i^{-1}$. (b)–(d) Spatial regions (black) where the indicator is (b) $|E_y|/|B_{xz}|$ less than its 10th percentile, or (c) δE_y or (d) H greater than its 90th percentile.

To demonstrate how $J_\parallel E_{so,\parallel}$ is sensitive to the indicators, we numerically calculate the average value of $\langle J_\parallel E_{so,\parallel}\rangle$ for each percentile of X. The percentile is calculated over the whole domain for $t > \tau$. Figure 9 shows $\langle J_\parallel E_{so,\parallel}\rangle$ normalized by its average value over the whole domain at $t > \tau$ as a function of the percentile of δE_y, $|E_y|/|B_{xz}|$, and H. The value of $\langle J_\parallel E_{so,\parallel}\rangle$ becomes larger when the percentile of $|E_y|/|B_{xz}|$, δE_y, or H is higher. The regions with one of $|E_y|/|B_{xz}|$ higher than the 89th percentile, δE_y higher than the 90th percentile, or H higher than the 93rd percentile are responsible for 50% of the energy conversion. Figures 8(b)–(d) show the regions selected by the values of $|E_y|/|B_{xz}|$ (b), δE_y (c), and H (d) higher than their 90th percentile by black coloring. The conversion sites selected by these indicators have either strongly positive or negative $J_\parallel E_{so,\parallel}$. The regions selected by these three indicators are quite different. The regions selected by $|E_y|/|B_{xz}|$ are relatively contiguous. They are concentrated near the reconnection sites and away from the centers of magnetic islands. This is useful because, as noted above, the magnetic islands provide very little net energy conversion to the particles. H selects both regions near the reconnection sites and centers of magnetic islands, though the latter make very little contribution to the net energy conversion. The regions selected by δE_y are scattered quite broadly but statistically concentrated around the reconnection sites.

4. Discussion and Summary

We have run 2.5D simulations of decaying turbulence. There are two phases of the simulations that give two distinct mechanisms of magnetic energy conversion. These phases are significantly modified by the magnitude of the guide field. As

Table 4
Indicators X and a Measure of Their Predictive Power, S_X, Based on the Fraction of the Energy Conversion $J_{\parallel}E_{\mathrm{so},\parallel}$ that Occurs in the Region with X Greater Than Its Median X_m

Indicator	Formula	S_X
Magnitude of parallel current	$\lvert \boldsymbol{J}_{\parallel} \rvert$	0.9
Magnitude of ratio of out-of-plane electric field to in-plane magnetic field	$\lvert E_y \rvert / \lvert B_{xz} \rvert$	0.82
Magnitude of parallel component of solenoidal electric field	$\lvert \boldsymbol{E}_{\mathrm{so},\parallel} \rvert$	0.8
Magnitude of y-component of nonideal electric field	$\delta E_y = \lvert \boldsymbol{E}_y + (\boldsymbol{U} \times \boldsymbol{B})_{y,\mathrm{so}} \rvert$	0.8
Estimate of current helicity	$H = \lvert \boldsymbol{B} \cdot \nabla \times \boldsymbol{B} / \mu_0 \rvert$	0.76
Magnitude of in-plane component of magnetic fluctuation	$\lvert B_x^2 + B_z^2 \rvert$	0.46
Magnitude of vorticity	$\lvert \nabla \times \boldsymbol{U} \rvert$	0.46
Magnitude of solenoidal component of nonideal electric field	$\lvert \boldsymbol{E}_{\mathrm{so}} + (\boldsymbol{U} \times \boldsymbol{B})_{\mathrm{so}} \rvert$	0.36
Magnitude of nonideal electric field	$\lvert \boldsymbol{E} + \boldsymbol{U} \times \boldsymbol{B} \rvert$	0.34
Divergence of bulk velocity	$\nabla \cdot \boldsymbol{U}$	0.26
Magnitude of cross helicity	$\lvert \boldsymbol{U} \cdot (\boldsymbol{B} - B_0 \hat{y}) \rvert$	0.1
Magnitude of y-component of magnetic fluctuation	$\lvert B_y - B_0 \rvert$	0.06
Magnitude of curvature of magnetic field	$\lvert \hat{\boldsymbol{B}} \cdot \nabla \hat{\boldsymbol{B}} \rvert$	0.06
Magnitude of magnetic helicity	$\lvert \boldsymbol{A} \cdot \boldsymbol{B} \rvert$	0.06
Magnitude of magnetic field	$\lvert B \rvert$	0

Note. $|\mathrm{J}_{\parallel}|$ and $|\mathrm{E}_{\mathrm{so},\parallel}|$ themselves, indicated in italics, are included for comparison purposes

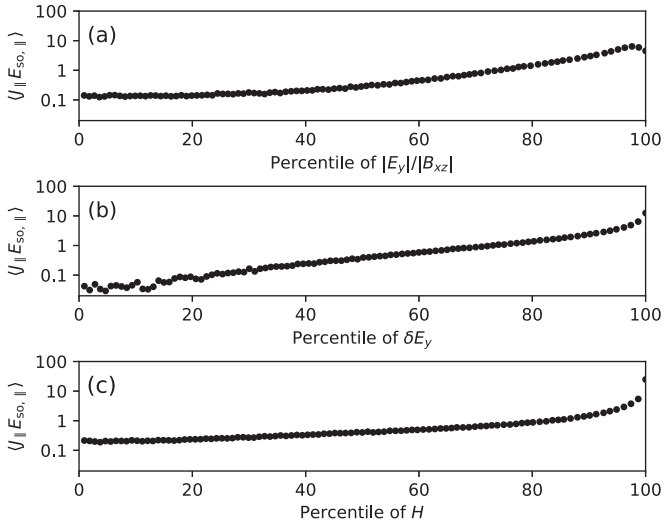

Figure 9. The average of $J_{\parallel}E_{\mathrm{so}\parallel}$ normalized by its average value as a function of percentile of (a) $|E_y|/|B_{\mathrm{xz}}|$, (b) δE_y, and (c) H with $B_0/b_0 = 2$ for $t > \tau$.

B_0 is higher, plasma becomes less compressible as the magnetic field partially confines the particles. Another effect of higher B_0 is the larger amplitude of the irrotational electric field. This field component is not directly responsible for the magnetic energy conversion and we therefore focus on the solenoidal electric field when searching for indicators of energy conversion locations.

For $t < \tau$ or the island-forming phase, plasma current structures contract to form magnetic islands. In this phase, electron motions take energy out of the magnetic field but also lose a large amount of energy to ions via the irrotational electric field. While the in-plane magnetic field becomes weaker, the out-of-plane component becomes stronger at centers of magnetic islands by taking energy from the in-plane particle motions. The current contraction obviously depends on the magnitude of the guide magnetic field. As B_0 gets stronger, the fractional energy conversion in this phase is weaker, and the ratio of energy taken out of the in-plane magnetic field by electrons to ions becomes higher. The irrotational electric field becomes stronger and is responsible for more energy transfer from electrons to ions. Both ions and electrons lose more energy to build strong B_y at centers of magnetic islands.

At $t > \tau$ or the decaying phase, the magnetic islands merge. During island merging, the magnetic reconnection inevitably occurs. As B_0 is higher, the particle parallel motion becomes dominant at taking energy out of the in-plane magnetic field (Wan et al. 2012; Makwana et al. 2017), and while ions gain more energy from the magnetic field, they lose a large amount of energy to electrons via the irrotational electric field. Electrons eventually gain more energy in this phase. Overall electrons become more effective at extracting the electromagnetic energy when B_0 is higher (Shay et al. 2018). This result is similar to the beta effect on the particle heating (Parashar et al. 2018).

The energy conversion is mainly mediated by the parallel component of the solenoidal electric field via $J_{\parallel}E_{\mathrm{so},\parallel}$, which is highly localized. Three particularly useful indicators of the regions of strong energy conversion are found. They are (1) the ratio of the out-of-plane electric field to the in-plane magnetic field (related to the suggestion by Lapenta 2021), (2) the out-of-plane component of the nonideal electric field, and (3) the magnitude of an estimate of current helicity. All of them select regions near the magnetic reconnection sites as locations of net energy conversion. Among them, $|E_y|/|B_{\mathrm{xz}}|$ provides regions that are most contiguous and tied with multiple reconnection sites. We propose that any mechanisms involving these indicators should receive particular attention in order to gain more insight on how magnetic energy is converted to bulk and thermal motions in turbulence with a strong guide field.

P.P. and D.R. would like to thank Thailand Science Research and Innovation for support through grant RTA 6280002. F. G. and S. D. acknowledge NASA programs with grant nos. 80HQTR20T0040 and 80HQTR21T0087, as well as DOE through the LDRD program at LANL and Office of Fusion Energy Sciences. F. G. also acknowledges support from DOE grant DE-SC0020219. This work was financially supported by the Office of the Permanent Secretary, Ministry of Higher Education, Science, Research and Innovation (Thailand) through grant No. RGNS 63-045 and was partly supported by the International Atomic Energy Agency (IAEA) under Contract No. 22785.

ORCID iDs

Peera Pongkitiwanichakul https://orcid.org/0000-0002-6609-1422
David Ruffolo https://orcid.org/0000-0003-3414-9666
Fan Guo https://orcid.org/0000-0003-4315-3755
Senbei Du https://orcid.org/0000-0003-1134-3909
Kittipat Malakit https://orcid.org/0000-0002-0915-5979

References

Bowers, K. J., Albright, B. J., Yin, L., Bergen, B., & Kwan, T. J. T. 2008, PhPl, 15, 055703

Camporeale, E., Sorriso-Valvo, L., Califano, F., & Retinò, A. 2018, PhRvL, 120, 125101
Chandran, B. D. G., Li, B., Rogers, B. N., Quataert, E., & Germaschewski, K. 2010, ApJ, 720, 503
Chen, B., Shen, C., Gary, D. E., et al. 2020, NatAs, 4, 1140
Comisso, L., & Sironi, L. 2018, PhRvL, 121, 255101
Dahlin, J. T., Drake, J. F., & Swisdak, M. 2014, PhPl, 21, 092304
Daughton, W., Roytershteyn, V., Karimabadi, H., et al. 2011, NatPh, 7, 539
De Pontieu, B., McIntosh, S. W., Carlsson, M., et al. 2007, Sci, 318, 1574
Du, S., Guo, F., Zank, G. P., Li, X., & Stanier, A. 2018, ApJ, 867, 16
Du, S., Zank, G. P., Li, X., & Guo, F. 2020, PhRvE, 101, 033208
Fu, X., Guo, F., Li, H., & Li, X. 2020, ApJ, 890, 161
Gary, S. P., & Borovsky, J. E. 2004, JGRA, 109, A06105
Gary, S. P., Hughes, R. S., & Wang, J. 2016, ApJ, 816, 102
Guo, F., Li, H., Daughton, W., & Liu, Y.-H. 2014, PhRvL, 113, 155005
Guo, F., Li, X., Daughton, W., et al. 2019, ApJL, 879, L23
Guo, F., Li, X., Daughton, W., et al. 2021, ApJ, 919, 111
Guo, F., Liu, Y.-H., Daughton, W., & Li, H. 2015, ApJ, 806, 167
Guo, F., Liu, Y.-H., Li, X., et al. 2020, PhPl, 27, 080501
Hughes, R. S., Gary, S. P., Wang, J., & Parashar, T. N. 2017, ApJL, 847, L14
Kida, S., & Orszag, S. A. 1992, JSCom, 7, 1
Lapenta, G. 2021, ApJ, 911, 147
Leamon, R. J., Matthaeus, W. H., Smith, C. W., & Wong, H. K. 1998, ApJL, 507, L181
Li, X., Guo, F., & Li, H. 2019a, ApJ, 879, 5
Li, X., Guo, F., Li, H., & Birn, J. 2018, ApJ, 855, 80
Li, X., Guo, F., Li, H., & Li, G. 2017, ApJ, 843, 21
Li, X., Guo, F., Li, H., Stanier, A., & Kilian, P. 2019b, ApJ, 884, 118
Makwana, K., Li, H., Guo, F., & Li, X. 2017, JPhCS, 837, 012004
Montgomery, D. 1982, PhST, 2A, 83
Parashar, T. N., Matthaeus, W. H., & Shay, M. A. 2018, ApJL, 864, L21
Parashar, T. N., Salem, C., Wicks, R. T., et al. 2015, JPlPh, 81, 905810513
Parker, E. N. 1988, ApJ, 330, 474
Perri, S., Goldstein, M. L., Dorelli, J. C., & Sahraoui, F. 2012, PhRvL, 109, 191101
Pongkitiwanichakul, P., Cattaneo, F., Boldyrev, S., Mason, J., & Perez, J. C. 2015, MNRAS, 454, 1503
Sahraoui, F., Goldstein, M. L., Robert, P., & Khotyaintsev, Y. V. 2009, PhRvL, 102, 231102
Shay, M. A., Haggerty, C. C., Matthaeus, W. H., et al. 2018, PhPl, 25, 012304
TenBarge, J. M., & Howes, G. G. 2013, ApJL, 771, L27
Van Ballegooijen, A. A. 1986, ApJ, 311, 1001
Wan, M., Matthaeus, W. H., Karimabadi, H., et al. 2012, PhRvL, 109, 195001
Wan, M., Matthaeus, W. H., Roytershteyn, V., et al. 2015, PhRvL, 114, 175002
Wu, P., Wan, M., Matthaeus, W. H., Shay, M. A., & Swisdak, M. 2013, PhRvL, 111, 121105
Yang, Y., Matthaeus, W. H., Parashar, T. N., et al. 2017a, PhPl, 24, 072306
Yang, Y., Matthaeus, W. H., Parashar, T. N., et al. 2017b, PhRvE, 95, 061201
Yang, Y., Wan, M., Matthaeus, W. H., & Chen, S. 2021, JFM, 916, A4
Zhang, H., Chen, X., Böttcher, M., Guo, F., & Li, H. 2015, ApJ, 804, 58
Zhang, H., Li, X., Giannios, D., et al. 2020, ApJ, 901, 149
Zhang, H., Li, X., Guo, F., & Giannios, D. 2018, ApJL, 862, L25
Zhdankin, V., Uzdensky, D. A., Werner, G. R., & Begelman, M. C. 2019, PhRvL, 122, 055101